Ilorin Journal of Science
FAPSCON 2024 PROCEEDINGS, 2024, pp. 97 – 110 (Printed in Nigeria)
ISSN: 2408 – 4840 © 2024 Faculty of Physical Sciences, University of Ilorin
https://doi.org/10.54908/iljs.fapscon.2024.11.03.1013

ILORIN JOURNAL OF SCEINCE

ILJS-24-063 (SPECIAL EDITION)

In-Silico Analysis of Molecular Modeling and Prediction of ADME/Tox Properties of 2,4-dinitro-N-[(E)-[(E)-3-(2-nitropenyl)prop-2-enyildene]amino]aniline Hydrazone (DNEAA) and its Manganese (II) Metal Complex as Potential Inhibitors of SARS-CoV-2 Protease

Eberendu K. O.[1*], Otuokere I. E.[2] and Nnaji J. C.[2]

[1]Department of Chemical Sciences, Faculty of Natural and Applied Sciences, Spiritan University, Nneochi, Abia, Nigeria
[2]Department of Chemistry, College of Physical and Applied Sciences, Michael Okpara University of Agriculture, Abia, Nigeria

Abstract

The emergence of severe acute respiratory syndrome coronavirus 2 (SARS-CoV-2) as the source of the worldwide coronavirus disease (COVID-19) pandemic has highlighted the importance of creating innovative medicines as long-term solutions to battle coronaviruses (CoVs). The goal of this research is to create a new hydrazone ligand and its metal complex, characterize the synthesized compounds using appropriate physical and spectroscopic techniques, and perform molecular docking, molecular dynamics simulations, and ADMETOX property prediction to gain a meaningful understanding of their biomolecular interactions. The findings suggested that LEU-37, HIS-100 VAL11, GLN 13, GLU46, LEU 12, VAL-15, VAL-25, and GLU-48 may play roles in the interaction of DNEAA and [Mn-(DNEAA)] with the active site of SARS-CoV-2. We therefore propose that the ligand (DNEAA) and its Mn(II) complex are strong inhibitors of the pathogenic NSP1 of the SARS-CoV-2 protease based on thorough in silico analysis.
Keyword: Non-structural protein 1, Drug discovery, Protein-ligand interaction, Drug-likeliness Prediction

1. Introduction

The extremely contagious characteristics of SARS-CoV-2 and its rapid transmission from person to person by droplets or direct conversation are major concerns for all sectors of society globally [1]. Non-structural protein 1 (NSP1), a unique and conserved viral leader protein, is a crucial virulence factor that impedes the release of interferon (IFN), breaks down host mRNA, and blocks host antiviral signaling pathways. Because of its vital involvement in the CoV life cycle, a unique viral Nsp1 is regarded as an accessible target for the creation of antiviral medications. Through fragment-based screening with X-ray crystallography, a variety of fragment hits against the SARS-CoV-2 NSP1 N-terminal domain were discovered.

Non-structural protein 1 (NSP1), a key virulence component, is a conserve d protein that degrades host mRNA, suppresses host antiviral signaling pathways, and prevents the production of interferon (IFN). The atomic resolution structure of NSP1 (0.99 Å) has been shown in Fig. 1.

Corresponding Author: Eberendu K.O
Email: eberendu.kizito@mouau.edu.ng

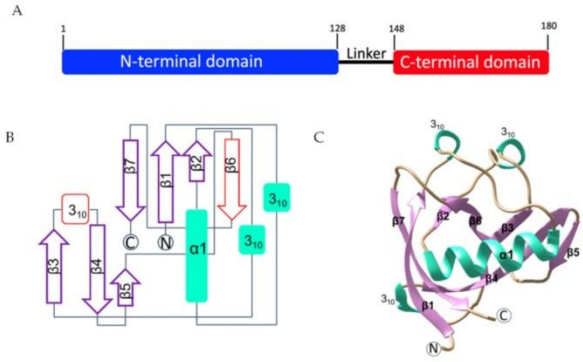

Figure 1. The structure of SARS-CoV-2 nsp110-126. (A) Bar diagram of the nsp1 domain arrangement, including the N-terminal domain (blue), the flexible linker region (black) and the C-terminal domain (red). (B) Topological arrangement of SARS-CoV-2 nsp110-126 at high resolution, where newly identified structural features are coloured in red. (C) Cartoon representation of the structure.

The secondary structure elements are depicted in different colours in the right panel with α-helixes coloured in green, ß-strands shaded in purple, and loops are shown in tan [2].

Near the end of 2019, a brand-new coronavirus was discovered [3]. Its emergence gave rise to the COVID-19 pandemic, which caused great concern among the public due to its high pollution level, ability to spread, and high death rate. The cause of this terrible illness, COVID-19, is a member of the beta coronavirus family, which has 89.1% nucleotide similarity with the SARS-CoV virus [4]. Actions were taken to stop the COVID-19 virus from spreading [5]. The literature has demonstrated that SARS-COVID-19 has been treated with the authorized antimalarial and autoimmune disease medications chloroquine (CQ) and hydroxychloroquine (HCQ), which are known to limit viral infection by increasing endosomal pH [6, 7, 8]. Additionally, remdesivir (RDV) and its active metabolites, GS441524, have been shown to be effective in the clinic when used together to limit the growth of SARS-CoV-2 [7], [9], [10], and [11]. Arbidol (ARB, umifenovir), a commercially available broad-spectrum antiviral medication that is categorized as a virus-host cell fusion inhibitor, has started a clinical trial to treat COVID-19 [12], [13]. Computational chemists have been deeply concerned with the virtual creation of compounds that can inhibit the virulent action of SARS-CoV-2. Based on this concern, we have used in silico techniques to analyze a novel aniline hydrazone ligand, DNEAA, as a potential pharmaceutical to block the pathogenic activities of SARS-CoV-2's NSP1. Hydrazones are one of the many organic molecules with a wide range of applications, and they have served as a strong hub for productive research. One crucial feature of pharmaceuticals is the C=N double bond seen in hydrazones [14]. The chemistry of hydrazone compounds combining O, N, and S donor ligands has drawn special attention due to their ability to coordinate as well as their biological functions [15]. Using hydrazones offers a chance to improve drug delivery by releasing the medication at targeted sites, including thrombosis or tumor tissue. Many scientists are working to find the best methods for producing these hydrazones, especially using heat and chemical catalysts. Just two of the numerous distinctive qualities of hydrazones that make them valuable in drug development are their capacity to react to different pH conditions and their simplicity in synthesis when combined with particular functional groups. Numerous studies have shown that the lone pair of electrons on the trigonally oriented nitrogen atom of the C=N group of hydrazones is what is responsible for their chemical and biological activity [17]. This flexibility makes them useful in a wide range of applications, including chelating agents, anti-inflammatory drugs, and anticancer drugs [16]. The biological uses of hydrazones and their derivatives as anti-oxidants, anti-consultants, analgesics, anti-microbial, anti-protozoals, anti-parasitic, anti-platelets, cardio-protective, anti-helminthic, anti-diabetic, anti-tubercular, anti-HIV, and so forth are among the other documented applications for these compounds [18]. The emphasized bioactivities of hydrazones and their corresponding metal complexes have generated curiosity regarding the creation of a novel

hydrazone, which will undergo bioactivity testing against SARS-CoV-2 [19]. Consequently, the reason we are doing this computational work with the novel compounds is to find important amino acid residues in the substrate-binding pocket that we can use for structure-based drug design. This will allow us to repurpose the other class of molecules and use the molecules as a template for the development of new inhibitors.

1. Materials and Methods

Preparation of the ligand

This experiment utilized only analytical-grade chemicals and reagents, imported from Sigma Aldrich, and were used without further treatment. The chemicals include pure 2:4-dinitrophenylhydrazine, (2,4-DNP), and 3-(2-nitrophenyl)prop-2-enal. DNEAA was prepared in the manner described in previous publications [20], [14]. To the clear solution obtained by filtering a warmed mixture of 2 g (0.01 mol.) of 2,4-DNP, 10 ml. of concentrated H_2SO4, 15 ml. of water, and 25 ml. of methanol, 2 g (0.01 mol.) of the carbonyl compound 3-(2-nitrophenyl)prop-2-enal was added and heated just to boiling. The precipitates formed were allowed to cool to room temperature before they were recrystallized from methanol and dried.

Preparation of the Metal Complex

The manganese (II) metal complex of the DNEAA hydrazone ligand was prepared by the direct reaction method; 2 g of $MnCl_2.4H_2O$ was dissolved in 5 ml of methanol, and the mixtures were stirred for about 5 min. A solution of the hydrazone ligand obtained by dissolving 2 g of the DNEAA ligand separately in a hot solution of methanol solvent was added to the solution of the metal salts and stirred. The obtained product was cooled, re-crystallized with methanol solvent, and dried at room temperature.

Determination of Physical Properties and Characterization Techniques

The melting point was recorded using Mettler Toledo's MT 211 melting point apparatus from Mettler Company. Elemental analysis was determined using an EA 2400 Series II. A solubility check was carried out in common solvents (DMF, DMSO, water, ethanol, and methanol) at 25 °C using 1 g of DNEAA. The measurement of the solid-state DC electrical conductance of the ligand and its complexes was carried out in their compressed pellet form (3 cm^{-2}), from room temperature to about 410 K.The electronic spectra of the DNEAA ligand and metal complex in DMSO were recorded on a Varian DMS 100 UV-visible double-beam spectrophotometer at room temperature. Magnetic susceptibilities were measured at room temperature on a Gouy balance using Hg[Co(CNS)]4 as calibrate. The "KBr Pellet Technique" was used to record the infrared spectra of DNEAA and metal complex on a Perkin-Elmer (Model C91158) IR spectrophotometer. Thermal measurements were carried out using a Perkin-Elmer TGA-7DSC-PYRIS-1-DTA-7 thermal analyzer maintained at a 10 °C/min heating rate. The NMR spectrum of DNEAA was recorded using a JEOL GSX-400 spectrometer. The mass spectrum of the new compounds were also recorded through electron spray ionization mass spectrometry.

Molecular Docking and Dynamics Simulations

Docking of the test compounds into the coordinates of 7K3N's crystal structures were carried out along with binding affinity assessments using AutoDock Vina, which was constructed in the PyRx software. The structures of the DNEAA were drawn using ChemDraw version 18.0 from PerkinElmer Informatics, Inc. The 7K3N's coordinates were made available from the protein data bank. The default settings of the ArgusLab 4.0.1 software were utilized to prepare the protein and ligand structures (proteins and cofactors are given the missing hydrogen atoms by fully preparing the protein and ligand at a neutral pH and an active site size of 6.0, which also assigns the protein residues their ideal ionization states). On Flare, the receptors and ligands were reduced by employing the XED accurate technique. The genetic algorithm-based method was used for the docking calculation because it is very accurate yet slow and does three separate docking runs to obtain the

lowest computed binding energy. All docked complexes' bond lengths, types of interactions, and three-dimensional images were all visualized using Protein-Plus and the Protein-Ligand Interaction Profiler Servers. The quality of the interactions between the biomolecules was assessed using binding affinity analysis.

Molecular dynamic simulations were performed for 150 nanoseconds by Desmond Schrodinger LLC [21]. By integrating Newton's classical equation of motion, MD simulations typically compute atom movements over time [22], [23]. The receptor-ligand complex was preprocessed using Maestro's Protein Preparation Wizard, which includes complex optimization and minimization. All systems were created using the System Builder tool. Transferable Intermolecular Interaction Potential 3 Points (TIP3P), a solvent model with an orthorhombic box, were selected using the OPLS 2005 force field [24]. Counterions were incorporated to ensure that the models were neutral. To simulate physiological circumstances, 0.15 M sodium chloride (NaCl) was used. The NPT ensemble with a 300 K temperature and 1 atm pressure was chosen for the entire simulation. The models were relaxed before the simulation. The paths were preserved for analysis at 100 ps intervals, and the simulation's stability was confirmed by comparing the protein and ligand root mean square deviation (RMSD) across time.

Prediction of ADMETox Properties, Substance Similarity and Bioacitvity

Using Simulations Plus, Inc.'s ADMET predictor v.9.5 in Lancaster, California, in silico ADMET investigations were carried out. The software received the SMILES code for the compound and uploaded it for evaluation. The physicochemical, metabolic, and toxicological characteristics of the compounds were assessed using the ADMET tool at a slightly neutral pH.Through an online tool called SimilarityLab, quick examination of druglike similarity and structure-activity relationship profiles was made possible.

The potential bioactivity of the docked DNEAA-7K3N complex was evaluated using PASS, an online web tool. The chemical structure of DNEAA, which was drawn using Chem Sketch software, was converted into mol files. These mole files were dropped into the handle provided on the server. After inputting the molecule, the biological activity prediction was then initiated by clicking on the "Get-Prediction" button below the drawing area.

3. Results

The analytical data of the DNEAA and complex are presented in Table 1, which indicates 1:1 stoichiometry, while the spectroscopic data are presented in Table 2. Thermogravimetric data for the primary ligand DNEAA (Fig. 2 A), and the synthesized metal complex (Fig. 2 B) are presented in Table 3. The cumulative weight losses of metal complexes at 150 °C and 200 °C are presented in Table 4. The information regarding the geometry of these complexes is obtained from their electronic data and magnetic moments, which are presented in Table 5. Table 6 and 7 present the results of molecular docking operation. The results of the molecular dynamics simulation of the ligand are presented in Figure 2, while the results of the allosteric modulators' in-Silico ADME/Tox evaluation for DNEAA and [Mn-(DNEAA)] are displayed in Tables 8 and 9.

Table 1: Analytical Data and Some Physical Properties of the Compounds

Compound	Molecular Formular	Molecular weight ($gmol^{-1}$)	Colour	Melting Point (^0C)	Yield (%)	Composition of elements (%) (Calc.)					Molar Conductance ohm-1 cm2 mol-1
						M	C	H	O	N	
DNEAA	$C_{15}H_{11}N_5O_6$	312.36	Yellowish-red	115 (95-120)	91	-	50.43 (50.36)	3.10 (4.00)	19.60 (20.36)	4.52 (4.81)	-

[Mn-(DNEAA)]	470.45	Whitish-grey	190 (170-250)	90	18.76 (18.72)	42.06 (41.57)	4.14 (4.72)	30.58 (30.54)	4.46 (5.6)		42

Table 2: Spectroscopic Data of the Compounds

FTIR			^{1}HNMR		^{13}CNMR		ESI MS	
Vibration frequency (cm-1)		**Assignments**	**δ (ppm)**	**Functional groups**	**δ (ppm)**	**Functional groups**	**m/z**	**Ion (100 %)**
L	**M**							
2079.9	-	(=CH) (alkene)	9.1,d	N=C-H	124.5-147.9	C=C Ar. (1)	357 470	M^+ (L) M^+ (M)
3063.9	-	(=C-H) (str.)	6.4, d	H–C=C	71.7-139.5	C=C Ar. (2)		
900.1	-	(=C-H) (bend).	7.5, m	Ar-H	128.4	C=C Conj. Alkene		
3324.8	-	(-N-H)	11.9, s	N-H	156.6	C=N- Azomethine		
1636.3	-	(-C=N)			143.2	C=N- for M		
-	1621.4	(-C=N) for M						
-	3446	(O-H, water)						
-	736	(M-Cl)						

L = DNEAA, M= [Mn-(DNEAA)]

Table 3: Cumulative % Weight Loss Data of the Ligand and its Metal Complex at Various Temperatures

Compound	**% Weight Loss at temperature (^{0}C)**											
	50	100	150	200	250	300	350	400	450	500	550	600
DNEAA	0.2	0.5	0.9	1.2	35	78	84	87	89	89	89	89
[M(DNEAA)]	0.1	0.2	0.2	0.5	1.5	4.9	65.7	70.2	73	75	75	75

Table 4: Cumulative Weight Loss Data of Metal Complex at 5 ^{0}C to 300 ^{0}C

Compound	**% Weight Loss at temperature (^{0}C)**											
	50 ^{0}C		100 ^{0}C		150 ^{0}C		200 ^{0}C		250 ^{0}C		300 ^{0}C	
	gm	%	gm	%	gm	%	gm	%	gm	%	gm	%
[M(DNEAA)]	0.31	0.1	0.32	0.1	0.63	0.2	1.8	0.5	4.80	1.5	5.42	2.0

Table 5: Electronic Spectra, Magnetic Moment Data, and Parameters for the Compounds

Compound	**Absorption region (cm-1)**	**Band assignment**	**Magnetic moment µeff (B.M.)**	**Geometry**	**d-d transition (cm^{-1})**			**Dq (cm^{-1})**	**B (cm^{-1})**	**ß=B/B^0**	**ß^0 (%)**
					υ_2	**υ_3**	**υ_4**				

DNEAA	379	$\pi - \pi^*$ (ILCT)	-	-	-	-	-	-	-	-	-
[Mn(DNEAA)]	320 510 710	$\pi - \pi^*$ LMCT E-T_2	5.92	Octahedral	4950	5406	12648	4505	187	0.23	79

Table 6: Molecular Docking Parameters

Compound	Binding Affinity Kcal/mol.	Mode (Pose)	RMSD	
			Upper bound	Lower bound
DNEAA	-10.3	2	1.251	4.50
[Mn-DNEAA]	-9.5	4	1.65	4.56

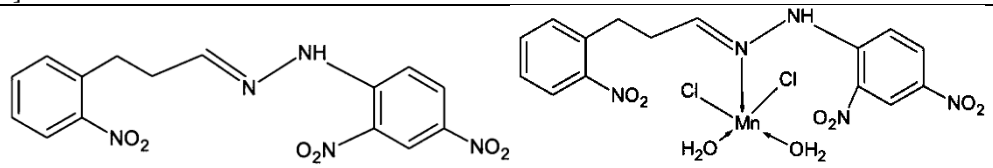

Figures 2 A and B. A. B.

Table 7: Interactions for DNEAA-7K3N

	Hydrophobic Interactions					Hydrogen bonding Interactions				
Index	**Residue**		**AA**	**Distance (Å)**		**Residue**		**AA**	**Distance (Å)**	
	L	**M**		**L**	**M**	**L**	**M**		**L**	**M**
1	12A	14A	LEU	3.34	3.36	11A	13A	VAL	3.1	3.08
2	13A	46A	GLN	3.23	3.28	13A	14A	GLN	3.2	3.21
3	14A	51A	VAL	3.66	3.67	13A	15A	GLN	3.3	3.33
4	46A	-	GLU	3.40	3.48	14A	15A	VAL	3.0	2.92
5	46A	-	GLU	3.56	3.58	46A	54A	GLU	2.9	3.0

Where L = Ligand, [Mn-(DNEAA)]

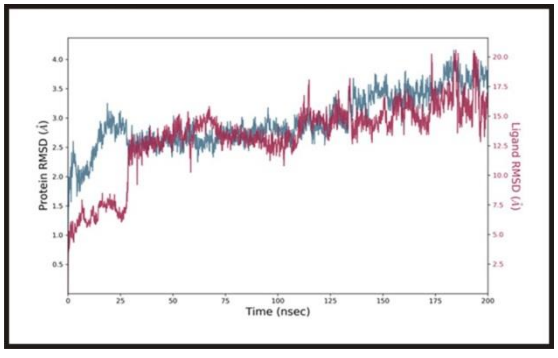

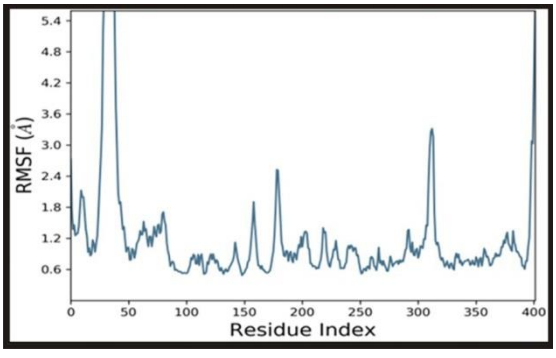

A. B.

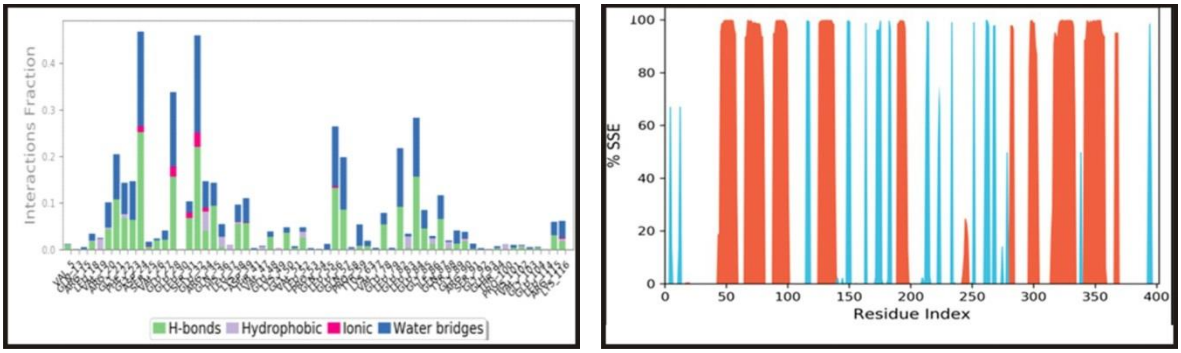

C. D.

Figure 2: A. Root mean square deviation (RMSD) of the C-alpha atoms of proteins and the ligand time. The change in protein RMSD over time was displayed on the left Y-axis. On the other hand, the ligand RMSD fluctuation over time was displayed on the right Y-axis. B. Residue-wise Root Mean Square Fluctuation (RMSF) of the protein complex with the DNEAA compound. C. Protein-ligand contact histogram of protein structures complexed with DNEAA. D. Protein Secondary Structure element. Alpha helices are represented by red columns, and beta strands by blue columns

Table 8: DNEAA's ADMET Parameters

Physicochemical Parameters			**ADME Parameters**			**Pharmacokinetics**		**Toxicity information**		**ReportedActivities**		
	Th-Value	**Obs.-value**		**Th-Value**	**Obs.-value**	HIA absorption	Yes	LD50 (mg/kg)	1600	Pa Ubiquinol-cytochrome-c reductase inhibitor	pi	
Mol. Weight (g/mol.)	<500	357.07	TPSA (Å²)	<140	131.85							
HB Acceptor	≤10	6	Water Sol. (mg/ml) SILICOS-IT, (x 10-3)	>1	2.03	BBB permeant	No	Toxicity Class	4	APOA1 expression enhancer	0.879	0.009
HB Donor	≤5	5	Bio. avai. score	≤0.55	0.55	P-gp substrate	No	Average similarity: (%)	38.68	Acrocylindropepsin inhibitor	0.793	0.004
Lipophilicity LogP	<5	3.2	Med. Chem. (PAIN) alert	105 molecules in library	0	CYP1A2 inhib.	No	Prediction accuracy: (%)	73	GSTP substrate	0.632	0.006
Molar refractivity	>30≤40	36.3	Synthetic accessibility	1(very easy) - 10 (very	3.51	CYP2C19 inhib.	No			CYP1A2 substrate	0.308	0.091

			difficu lt)						
No. of violation s or Rule of five	-	0		CYP2C 9 inhibito r	No		CYP19A1 expression inhibitor	0.3 37	0.0 70
				LogKp (skin perm.) (cm/s)	-6.1 7				

Th-Value: Threshold value. Obs.-value: Observed value

4. Discussion

Table 1 depicts the physical characteristics of the produced hydrazone, DNEAA, and its manganese complex. The ligand and metal complex are colorless, crystalline, and air-stable at room temperature. They do not dissolve in water, ethanol, or methanol but dissolve in dimethylformamide and dimethyl sulfoxide. The yields of the synthesized ligand is 91% whereas that of the metal complex is 90% (Table 1). This demonstrated that the syntheses were carried out efficiently. Experimental melting points are in accordance with theoretical values (in brackets). The metal complex's molar conductance (10^{-4} M) is within the range of non-electrolytes (42 $Ohm^{-1}cm^2mol^{-1}$), indicating that the anions are coordinated with the metal ion [25]. Spectroscopic data for the ligand and complex are shown in Table 2. In the IR data, bands observed in the range 2109.7–2079.9 cm^{-1} indicated the presence of the −CH group of alkenes in the ligand and metal complexes. The broad bands observed in the wave number range of 3369.5-3384 cm^{-1} were caused by the stretching frequency of the -NH group's hydrogen bonding in the ligand and metal complex. The stretching vibrations of the aromatic -CH group of the ligand and metal complex were observed at 3063.9 cm^{-1}, while the bending vibrations were observed at 920.7 - 872.2 cm^{-1}. Strong peaks detected at frequencies ranging from 1636.3 to 1591.6 cm^{-1} correspond to the vibrations of the ligand and metal complex's -C=N groups. Lowering the frequency to 1591.6 cm^{-1} demonstrated that the azomethine group actively participated in coordination [26], [27], and [28].

The 1HNMR data are shown in Table 2. The azomethine proton (-HC=N-) signal ranged from 8.76 to 9.3 ppm (d, $\delta = 9.1$ ppm). The symmetric structure of the azomethine carbon and its neighboring carbon was responsible for the proton's deshielding impact and the shift of its peak toward the lower field after 8.70 [29]. The N-H group was represented by a singlet signal at δ 11.89–12.0 (as expected for acidic protons), while aromatic protons were represented by multiplet peaks in the 7.5–8.0 region. Deshielding occurs in the plane of the C=C bond due to anisotropy and steric processes. These effects caused the observed signals at $\delta = 6.0–7.0$ ppm, which reflect the protons connected to the olefinic carbon (H-C=C-H). The effects of an electronegative nitrogen atom were clearly seen in the N-H peak, which was deshielded and shifted well downfield beyond 11.65 ppm. Furthermore, the two multiplets that occurred between 7.5 and 8.0 indicate the presence of two aromatic rings in the produced compounds, with protons resonating within the stated chemical shift. According to [30], "Mechanism of Spin-Orbit Effects on the NMR Chemical Shifts in Transition Metal Complexes, Paramagnetic NMR shielding and spin-orbit effects affect the character of the metal-ligand (M-L) bond." The signal for imine proton in the free ligand at δ 9.1 ppm shifts upfield to 8.7 in the [Mn-(DNEAA)] complex, indicating metal-nitrogen coordination. Table 2 shows ^{13}CNMR resonance data with δ. The signal from the carbon atom linked to the azomethine group in the ligand DNEAA was detected at δ 156.6 ppm. However, in the spectra of the corresponding metal complex, the shift in the ^{13}C resonance to δ 143.3 suggested that the nitrogen atom of the azomethine group coordinated with the central atom. The ligand's coordination with the

metal was demonstrated by a new δ value of 125.9, which was not present in the spctrum of the free ligand. The signal from aromatic ring carbons with different substitutions was detected in the range of δ 124.5–147.9 and 115.9–148.1 for the ligand and 71.7–139.5 for the metal complex.

Tables 3 and 4 show thermogravimetric data for the metal complex. The complex lost weight progressively during the experiment, then the sample experienced increased weight loss, and eventually, in the temperature range of 500–600 ºC, the rate of weight loss became considerably more moderate. During the early period, steady weight loss may be caused by water of hydration, which can be crystal or coordinated water. The fact that metal complexes decompose at a slower rate than ligands suggests the possibility of weak intermolecular hydrogen bonding. The greater percentage of loss found in the complex above 300 ºC implies that the complex is decomposing and has formed oxides.

The electronic data and magnetic moments reported in Table 5 provide more information on the complex's geometry. The free ligand (DNEAA) band at 379 nm was attributed to the π→π* transition of the azomethine moieties [31]. The metal complex ([Mn-(DNEAA)]) showed a shift in the π→π* transitions to 320 nm, possibly due to coordination with the metal center [32]. The ligand-to-metal transition (LMCT) was detected at 510 nm in the spectra of the [Mn-(DNEAA)] complex. The Mn(II) complex was discovered to be diamagnetic, as expected from six-coordinated d5 octahedral complexes. The measured transitions of the Mn(II) d5 complex provide B = 187 cm^{-1}, β = 0.23, and $ß_0$ = 79%. The E→T2 transitions for the Mn(II) complex in an octahedral environment are attributed to substantial crystal field splitting.

Table 6 shows the molecular docking results. Semi-empirical scoring functions were used to calculate the protein-ligand binding affinities, mode of binding, and RMSD values for the interactions of the ligand, DNEAA, and its metal complex with the crystallographic coordinates of the SARS-CoV-2 protease. The modes with the highest binding energies were chosen for the ligand-protein interaction study. As a result, the DNEAA-7K3N's interaction had the highest binding affinity (-10.3 kcal/mol), with two docking modes (poses) having lower and upper bound RMSD values of 1.15 and 4.50, respectively, whereas the metal complex interaction had the highest binding affinity (-9.5 kcal/mol), with four modes having lower and upper bound RMSD values of 1.65 and 4.51, respectively. This finding is consistent with that of [33], which emphasizes that the success rate of docking procedures is typically given as the percentage of test instances in the dataset for which the top scoring poses have RMSD up to 4.50. These data show that the lower the docking score, the greater the affinity.

A summary of the amino acids interacting with the ligand and complex at the allosteric binding sites has been presented in Tables 7. It was observed that in the interactions of SARS-CoV-2 with the test compounds, there are regions of electrophilic and nucleophilic reactivity trend, indicating that the presence of transition metal ions may have influenced the increase in charge density in protein based on the results obtained. The larger concentration of charges in the protein when interacting with metal complex and lower with DNEAA ligand is supported by the scoring function values obtained during docking operations for the ligand and metal complex, respectively [35].

In the molecular dynamic simulation of the ligand and metal complex, the RMSD plot clearly demonstrated that the proteins in the protein-ligand complex reached stability at 15 ns (Fig. 2A). The RMSD value variations remain within 3.0 Angstrom for the rest of the simulation. After attaining equilibrium, the RMSD values of DNEAA fit to protein fluctuated within 3.0 Angstrom up to 115 ns and remained stable for the rest of the simulation up to 150 ns, after which higher summits were determined at Angstrom 3.5. The root mean square fluctuation (RMSF) value of the proteins was compared to that of the test compound (Fig. 2B); residues with greater peaks belong to loop areas or N and C-terminal zones, as determined by MD trajectories. Low RMSF values for binding site residues indicate the stability of DNEAA binding to 7K3N. Figure 2C depicts the protein-ligand interaction histogram for the complex (DNEAA-7K3N). LEU-37 and HIS-100 were critical for

hydrophobic contacts, whereas VAL-15, VAL-25, and GLU-48 were significant for hydrogen bonding. The stacked bar charts were standardized throughout the trajectory, with a value of 1.0 indicating the specific interaction and remaining constant for the whole simulation time. Because some protein residues may have multiple interactions of the same subtype with the ligand, values above 1.0 are regarded as reliable. The secondary structure analysis (%SSE) revealed that the percentages of helix and strand in the protein-ligand complex (DNEAA-7K3N) were 10.92 percent and 4.53 percent, respectively, and the overall secondary structure components were 15.46 percent (Fig. 2D). The study of MD simulation results, including RMSD, RMSF, protein-ligand interaction fractions, and SSE of the docked complex, demonstrated that DNEAA was stable under physiological settings during the MD simulations. The computational simulations demonstrated that DNEAA can inhibit the designated targets, namely the NSP 1 of SARS-COV-2 enzymes, by creating stable hydrogen bonds [36].

Results for in silico ADME/Tox evaluation for DNEAA and [Mn-(DNEAA)] are displayed in Table 8 and 9. Lipinski's Rule of Five (RO5) drug likelihood test, which was conducted for the ligand and its metal complex, yielded zero violations for these properties. Topological surface area (TPSA) values were obtained for the ligand and its metal complex, and the results indicated that they would display bioactivity, as previously described by [37]. Water solubility values for DNEAA and [Mn-(DNEAA)], indicate that the compounds are projected to be water-soluble. The bioavailability ratings indicate that the compounds under study may be well absorbed in humans, with a projected bioavailability score ≤0.55, similar to previous investigations [38].

According to the medicinal chemistry-friendliness assessment, PAINS (for pan assay interference chemicals, also known as frequent hits or promiscuous compounds) are molecules having substructures that react strongly in assays regardless of the protein target. These pieces have been discovered to provide biological output that is mistakenly positive, as reported by [39]. DNEAA and [Mn-(DNEAA)] showed zero PAIN alerts, which means that they are free from such fragments. Synthetic accessibility (SA) scores for DNEAA and [Mn-(DNEAA)] are also given in Tables 8 and 9, which demonstrate the simplicity and viability of the compounds' synthetic pathways. According to the works of [40], the SA Score has a range from 1 (very simple) to 10 (very tough) after normalization.

Because of reduced clearance and accumulation of the medication or its metabolites, the inhibition isoenzymes (CYPs) is undeniably a key contributor to pharmacokinetics-related pharmaceutical interactions, resulting in toxic or other undesirable side effects of drugs [41], [42]. The models respond "yes" or "no" based on whether the target chemical is likely to inhibit a specific CYP. Results obtained from the present reseacrh demonstrate that the test substances are not inhibitors to the CYP isoenzymes being studied. The hypothesis that a molecule is less skin permeable as the log Kp (measured in cm/s) decreases has been described in the literature. The test substances' Kp values indicated that they are not expected to penetrate the skin under normal conditions. DNEAA and its metal complex were projected to be in toxicity class 4, implying that they could be dangerous if ingested at the specified levels orally.

A quick review of druglike similarities and structures, also known as activity relationship profiles, was carried out using the web service SimilarityLab. The Ultrafast Shape Recognition with CREDO Atom Types (USRCAT) algorithm has been widely used [43], and it already comprises over 12.7 million commercially accessible, unique druglike small compounds that can be searched using a 3D chemical similarity measure [44]. The results revealed two top targets that are similar to the substances under investigation: chlorhexidine (CID: 9552079) and nitenpyram (CID: 3034287). The former serves as an antiinfective and antibacterial agent, whereas the latter has been reported to function as a neonicotinoid insecticide [45].

Furthermore, the biological activity spectrum (BAS), which reflects various pharmacological effects, physiological and biochemical mechanisms of action, and specific toxicity (mutagenicity, carcinogenicity, teratogenicity, and embryotoxicity), is once again an intrinsic characteristic of a substance, implying that the

structure of a chemical substance has a significant impact on its action [46]. The PASS prediction method was used to forecast the activity of DNEAA and its metal complex, with the results presented in Tables 8 and 9. Using the findings of [47], the biological activity of each molecule was assessed using Pa > Pi and Pa > 0.7 (pa = % active; pi = % inactive) models. It was observed that the ubiquinol-cytochrome-c reductase inhibitor, acrocylindropepsin inhibitor, GST P substrate, APOA1 expression enhancer, CYP1A2 substrate, and CYP19A1 expression inhibitors all had Pa values greater than 0.7 for DNEAA and [Mn-(DNEAA)]. The current study's findings suggest that the PASS spectrum of DNEAA and its metal complex have remarkable pharmacological effects.

Conclusion

A new hydrazone ligand and its Mn(II) complex were produced, characterized, and structurally determined. The results of in silico molecular docking, dynamics, and ADMETox simulations clearly show that the synthesized compounds have very high binding affinities and the best poses (conformations) when they interact with the NSP1 of the SARS-CoV-2 protease, and could work well as medication to reduce the virulent symptoms of the infectious organism. DNEAA hydrazone and its metal complex have demonstrated the potential to be included in a list of various drugs that will be tested in pre-clinical and clinical settings for interactions with NSP1 in SARS-CoV-2. We thus propose that the ligand (DNEAA) and its Mn(II) complex ([Mn-(DNEAA)]) could be effective inhibitors of the pathogenic NSP1 of the SARS-CoV-2 protease.

Author Contributions: Supervision, I.E Otuokere; Writing, review and editing, J.C Nnaji

Acknowledgments: We are grateful to all who participated in the courses of actualizing and publishing this research article.

Disclosure statement:

The authors report there are no competing interests to declare.

References

1. Zhai P., Ding Y., Wu X., Long J., Zhong Y., Li Y. (2020).The epidemiology, diagnosis and treatment of COVID-19. Int J Antimicrob Agents,; 105955. https ://doi.org/10.1016/j.ijant imica g.2020.10595
2. Ma, S., Damfo, S., Lou, J., Pinotsis, N., Bowler, M.W., Haider, S., Kozielski, F. (2022). Two Ligand-Binding Sites on SARS-CoV-2 Non-Structural Protein 1 Revealed by Fragment- Based X-ray Screening. Int. J. Mol. Sci. 23(20), 12448. https://doi.org/10.3390/ijms232012448
3. Guo, Y., Cao Q.D., Hong Z.S., Tan Y.Y., Chen S.D., Jin H.J., Tan K.S., Wang D.Y.,Yan Y. (2022). The origin, transmission, and clinical therapies on coronavirus disease 2019 (COVID-19) outbreak an update on the status. Mil Med Res. 7(1), 11–11. https://doi.org/10.1186/s40779-020-00240-0
4. Beigel, J. H., Tomashek, K. M., Dodd, L. E., Mehta, A. K., Zingman, B. S., Kalil, A. C., Hohmann, E., Chu, H. Y., Luetkemeyer, A., Kline, S., Lopez de Castilla, D., Finberg, R. W., Dierberg, K., Tapson, V., Hsieh, L., Patterson, T. F., Paredes, R., Sweeney, D. A., Short, W. R., Touloumi, G., et al. (2020). Remdesivir for the Treatment of Covid-19 - Final Report. The New England journal of medicine. *383*(19), 1813–1826. https://doi.org/10.1056/NEJMoa2007764.
5. Lai, A. Y., Lee, L., Wang, M. P., Feng, Y., Lai, T. T., Ho, L. M., Lam, V. S., Ip, M. S., Lam, T. H. (2020). Mental Health Impacts of the COVID-19 Pandemic on International University Students, Related Stressors, and Coping Strategies. Frontiers in psychiatry, 11, 584240. https://doi.org/10.3389/fpsyt.2020.584240
6. Devaux, C. A., Rolain, J. M., Colson, P., Raoult, D. (2020). New insights on the antiviral effects of chloroquine against coronavirus: what to expect for COVID-19?. International journal of antimicrobial agents. *55*(5), 105938. https://doi.org/10.1016/j.ijantimicag.2020.105938
7. Touret F., de Lamballerie X. (2020). Of chloroquine and COVID-19. Antiviral Res 177:104762. https ://doi.org/10.1016/j.antiviral.2020.10476 2

8. Al-Bari M. (2017). Targeting endosomal acidification by chloroquine analogs as a promising strategy for the treatment of emerging viral diseases. Pharmacol Res Perspect. 5(1), 293–293. https ://doi.org/10.1002/prp2.293
9. Al-Tawfiq J.A., Al-Homoud A.H., and Memish Z.A. (2020). Remdesivir as a possible therapeutic option for the COVID-19. Travel Med Infect Dis. 10, 16-15. https ://doi.org/10.1016/j.tmaid
10. Morse, J.S., Lalonde, T., Xu, S., Liu, W.R. (2020). Learning from the Past: Possible Urgent Prevention and Treatment Options for Severe Acute Respiratory Infections Caused by 2019-nCoV. *Chembiochem:* European journal of chemical biology. *21*(5), 730–738. https://doi.org/10.1002/cbic.202000047.
11. Sheahan, T.P., Sims, A.C., Zhou, S., Graham, R. L., Pruijssers, A. J., Agostini, M. L., Leist, S. R., Schäfer, A., Dinnon, K. H., 3rd, Stevens, L. J., Chappell, J. D., Lu, X., Hughes, T. M., George, A. S., Hill, C. S., Montgomery, S. A., Brown, A. J., Bluemling, G. R., Natchus, M. G., Saindane, M., et al. (2020). An orally bioavailable broad-spectrum antiviral inhibits SARS-CoV-2 in human airway epithelial cell cultures and multiple coronaviruses in mice. Science translational medicine. *12*(541), eabb5883.https://doi.org/10.1126/scitranslmed.abb5883.
12. Boriskin, Y. S., Leneva, I. A., Pécheur, E. I., Polyak, S. J. (2008). Arbidol: a broad-spectrum antiviral compound that blocks viral fusion. Current medicinal chemistry. 15(10), 997–1005. https://doi.org/10.2174/092986708784049658.
13. He, D., Zhao, S., Xu, X., Lin, Q., Zhuang, Z., Cao, P., Wang, M.H., Lou, Y., Xiao, L., Wu, Y., Yang, L. (2020). Low dispersion in the infectiousness of COVID-19 cases implies difficulty in control. BMC Public Health. 20, 1558. https://doi.org/10.1186/s12889-020-09624-2.
14. Belskaya N.P., Dehaen W., Bakulev V.A. (2010). Synthesis and properties of hydrazones bearing amide, thioamide and amidine functions. Archival Organic Chemistry. 1, 275‑332. http://dx.doi.org/10.3998/ark.5550190.0011.108
15. Ramkisore U., Anamika U., Dikshit S.N. (2020). Synthesis and Spectroscopic Studies of Bivalent Transition Metal Complexes of Co(II), Ni(II), and Ti(II) with Hydrazide-Hydrazones. Journal of Emerging Technologies and Innovative Research (JETIR) 5(8), 1-5.
16. Wahbeh J., Milkowski S. (2019). The Use of Hydrazones for Biomedical Applications. SLAS Technolog. 24(2), 16-168.https://doi10.1177/2472630318822713.journals.sagepub.com/home/jla
17. Wang, X., Jaun Y., LI S., Guoping Z., Baoan S. (2019). Design, synthesis, and antibacterial activity of novel Schiff base derivatives of quinazolin-4(3H)-one. Eur J Med Chem, 22(77), 65-74. https://doi.org/10.1016/j.ejmech.2014.02.053
18. Zaidi, H.H.S, Abdul H., Abo N.B.R. (2018). Properties and Uses of Substituted Hydrazones. Journal of Pharmaceutical and Applied Chemistry, 4(1), 17-21. http://dx.doi.org/10.18576/jpac/040103
19. Radovic T. (2020). 'History of in silico biology, An overview'. Novel Global Community Educational Foundation. Australia. 1-43. http://dx.doi.org/10.13140/RG.2.2.11933.79841/1.
20. Otuokere, I.E., Chinweuba, A.J. (2011). Synthesis, Characterization and fungicidal activity of 3-chloro-4-methyl-N-[(1E)-1-phenylethylidene]aniline ligand and its metal complexes. Journal of Chemical and Pharmaceutical Research. 6(3), 905-911
21. Bowers KJaC David E., Xu Huafeng, Dror Ron O., Eastwood Michael P., Gregersen Brent A. (2006). Scalable Algorithms for Molecular Dynamics Simulations on Commodity Clusters: IEEE, 43–43
22. Hildebrand P.W., Rose A.S., Tiemann J.K.S. (2019). Bringing Molecular Dynamics Simulation Data into View. Trends Biochem Sci. 44: 902–913. https://doi.org/10.1016/j.tibs.2019.06.004 PMID: 31301982
23. Rasheed M.A., Iqbal M.N., Saddick S., Ali I., Khan F.S., et al. (2021). Identification of Lead Compounds against Scm (fms10) in Enterococcus faecium Using Computer Aided Drug Designing. Life (Basel) 11. https://doi.org/10.3390/life11020077 PMID: 33494233
24. Shivakumar D., Williams J., Wu Y., Damm W., Shelley J., et al. (2010). Prediction of Absolute SolvationFree Energies using Molecular Dynamics Free Energy Perturbation and the OPLS Force Field. Journalof Chemical Theory and Computation 6: 1509–1519. https://doi.org/10.1021/ct900587b PMID:26615687

25. Bakheit M., Satyanarayana S. (2010). Vitamin B12 Model complexes: synthesis and characterization of thiocyanato cobaloximes and thiocyanato bridged dicobaloximes of o-donor ligands: DNA Binding and antimicrobial activity. Journal of Korean Chemical Society. 54(6): 687-695.
26. Haba P., Farba B.T., Adama S.Y., Mamour S., Madina D., Ba, I.T., Thiam, M.G., Pascal R., Javier E., 2019. Synthesis, structural study and X-ray structure determination of transition metal complexes of 4-phenyl-1-(1-(pyridin-2-yl)ethylidene)thiosemicarbazide. Journal of Applied Chemistry (IOSR-JAC). 12(8), 2278-5736.
27. Abdelaaty A.S., Iqbal H., Aaqib U., Atta U.K., Wali U.K., Ullah U., Hafiz M. M (2019). Synthesis, Characterization and Biological Activities of Hydrazone Schiff Base and its Novel Metal Complexes. Sains Malaysiana. 48(7); 1439 – 1446.
28. Omoruyi G.I., Alexander P.S., Eric C.H. (2016). Metal Complexes of New Bioactive Pyrazolone Phenylhydrazones; Crystal Structure of 4-Acetyl-3-methyl-1-phenyl-2-pyrazoline-5-one phenylhydrazone Ampp-Ph. International Journal o f Molecular Sciences. 17: 687, 2-24.
29. Paweł G., Agnieszka P., Sonia K., Jan G., Mariola S., Henryk J., Sebastian M., Ewa S. (2019). Symmetrical and unsymmetrical azomethines with thiophene core: structure–properties investigations. Journal of Material Science 54: 13491–13508.
30. Vícha, J., Straka, M., Munzarová, M.L., Marek R. (**2**014). "Mechanism of Spin-Orbit Effects on the NMR Chemical Shift in Transition Metal Complexes: Linking NMR to EPR," JCTC. 10(6): 1021.
31. Beyazit N., Sergül Ç., Cahit D. (2017). Metal complexes of perimidine and Schiff base ligands bearing both naphthalene and chromone moieties: synthesis and catalytic activity. Bulgarian Chemical Communications. 49(I):115-12.
32. Tyagi M., Sulekh C., Prateek T., Jameel A., Arvind K., Baleswar S. (2017). Synthesis, characterization and anti-fungal evaluation of Ni(II) and Cu(II) complexes with a derivative of 4-aminoantipyrine. Journal of Taibah University for Science. 11(1): 110-120.
33. Nissink J.W.M., Chris M., Mike H., Marcel L.V., Jason C.C., Robin T. (2002). A new test set for validating predictions of protein-ligand interaction. PubMed. 1; 49(4): 457-71.
34. Ma, S., Damfo, S., Lou, J., Pinotsis, N., Bowler, M.W., Haider, S., Kozielski, F. (2022). Two Ligand-Binding Sites on SARS-CoV-2 Non-Structural Protein 1 Revealed by Fragment- Based X-ray Screening. Int. J. Mol. Sci. 23(20), 12448. https://doi.org/10.3390/ijms232012448
35. Wilson, D.N. (2014). Ribosome-targeting antibiotics and mechanisms of bacterial resistance. Nat. Rev. Microbiol.**,** 12: 35–48
36. Malik A., Iqbal M.N., Ashraf S., Khan M.S., Shahzadi S., Shafique M.F., et al. (2023). *In silico* elucidation of potential drug targets against oxygenase domain of Human eNOS Dysfunction. PLoS ONE. 18(4): e0284993. https://doi.org/10.1371/journal.pone.0284993
37. Prasanna S., Doerksen R.J. (2020). Topological Polar Surface Area: A Useful Descriptor in 2D-QSAR. Curr Med Chem 16(1), 21–41. https://doi.org/10.2174/092986709787002817
38. Yvonne C.M. (2005). A bioavailability score. J Med Chem, 48(9), 3164-7. https://doi.org/10.1021/jm0492002
39. Baell, J.B., Holloway, G.A. (2010). New substructure filters for removal of pan assay interference compounds (PAINS) from screening libraries and for their exclusion in bioassays. J. Med. Chem. 53, 2719–2740. https://doi.org/10.1021/jm901137j
40. Ertl, P., Schuffenhauer, A. (2009). Estimation of synthetic accessibility score of drug-like molecules based on molecular complexity and fragment contributions. J. Cheminform. 1, 8. https://doi.org/10.1186/1758-2946-1-8
41. Hollenberg, P.F. (2002). Characteristics and common properties of inhibitors, inducers, and activators of CYP enzymes. Drug Metab. Rev., 34, 17–35. https://doi.org/10.1081/dmr-120001387
42. Kirchmair J., Andreas H.G., Dieter L., Jens K., Bernard T., Ian D., Wilson, R.C.G., Gisbert S. (2015). Predicting drug metabolism: experiment and/or computation? Nature Rev. Drug Discov. 14, 387–404. https://doi.org/10.1038/nrd4581.

43. Schreyer, A.M., Blundell, T. (2012). USRCAT: Real-time ultrafast shape recognition with harmacophoric constraints. J. Cheminformatics. *4*, 27 https://doi.org/10.1186/1758- 2946-4-27
44. eMolecules. (2021). Available online: https://www.emolecules.com/ (accessed on 5 June 2021).
45. National Center for Biotechnology Information (NCBI). (2023). PubChem Compound Summary for CID 9552079, Chlorhexidine. Retrieved August 12, 2023 from https://pubchem.ncbi.nlm.nih.gov/compound/chlorhexidine
46. Justin K., Frederick P.R. (2008). Chemical substructures that enrich for biological activity. Bioinformatics. 24(21), 2518–2525. https://doi.org/10.1093/bioinformatics/btn479
47. Otuokere I.E., Onyinye U.A., Felix C.N., Chinedum, I.N., Joy N.E., Chiemela W., Ogbonna A.B. (2022). GC-MS Profiling and In Silico Studies to Identify Potential SARS-CoV-2 Nonstructural Protein Inhibitors from *Psidium guajava*. African Scientific RepszxazxyS sorts 1: 161–173. https://doi.org/10.46481/asr.2022.1.3.52
48. Otuokere I.E, Igwe K.K, Nwankwo C.I, Achi N.K, Asuquo I.G, and Eberendu K.O, (2024). Electrostatic Potential Mapped onto Electron Density Surface, ADME, Molecular Docking and Molecular Dynamics Simulations of Some Indolin-2- one Analogues as Cytochrome C Peroxidase Inhibitors. Research Square, PREPRINT (Version 1) available at Research Square [https://doi.org/10.21203/rs.3.rs-4200649/v1]
49. Amaku F.James, Otuokere I.E, and Igwe K.K, (2015). Molecular Mechanics Studies of a Psychostimulating Agent, 2-[(Diphenylmethyl) Sulfinyl] Acetamide (Modafinil). International Journal of Bioinformatics and Biomedical Engineering. Vol. 1, No. 3, 2015, pp. 256-262
50. Amako, N., & Nnaji, J. (2017). GC/MS ANALYSIS AND ANTIMICROBIAL ACTIVITY OF PENTACYCLIC TRITERPENOIDS ISOLATED FROM COMBRETUM GLUTINOSUM PERR. EX. DC. STEM BARK. Journal of Chemical Society of Nigeria, 41(2). Retrieved from http://journals.chemsociety.org.ng/index.php/jcsn/article/view/91
51. Nnaji, J. C., Uzairu, A, Harrison, G. F. S., and Balarabe, M. L., (2007). Evaluation Of Cadmium, Chromium, Copper, Lead and Zinc Concentrations in The Fish Head/Viscera Of Oreochromis Niloticus And Synodontis Schall Of River Galma, Zaria, Nigeria. Electronic Journal of environmental, Agricultural and Food Chemistry, 6 (10), 2420-2426
52. Eberendu K.O., and Otuokere I.E, (2016). Complexation Behavior of 1-Phenyl-2,3-Dimethyl-4-(Benzylamino) Pyrazol-5-One Schiff Base Ligand with Manganese Ion. Research Journal of Science and Technology, Vol 8, No 4 (2016), 199-203.